

Article

A Numerical Investigation of Dimensionless Numbers Characterizing Meltpool Morphology of the Laser Powder Bed Fusion Process

Kunal Bhagat  and Shiva Rudraraju * 

Department of Mechanical Engineering, University of Wisconsin-Madison, Madison, WI 53706, USA

* Correspondence: shiva.rudraraju@wisc.edu

Abstract: Microstructure evolution in metal additive manufacturing (AM) is a complex multi-physics and multi-scale problem. Understanding the impact of AM process conditions on the microstructure evolution and the resulting mechanical properties of the printed component remains an active area of research. At the meltpool scale, the thermo-fluidic governing equations have been extensively modeled in the literature to understand the meltpool conditions and the thermal gradients in its vicinity. In many phenomena governed by partial differential equations, dimensional analysis and identification of important dimensionless numbers can provide significant insights into the process dynamics. In this context, we present a novel strategy using dimensional analysis and the linear least-squares regression method to numerically investigate the thermo-fluidic governing equations of the Laser Powder Bed Fusion AM process. First, the governing equations are solved using the Finite Element Method, and the model predictions are validated by comparing with experimentally estimated cooling rates, and with numerical results from the literature. Then, through dimensional analysis, an important dimensionless quantity interpreted as a measure of heat absorbed by the powdered material and the meltpool, is identified. This dimensionless measure of absorbed heat, along with classical dimensionless quantities such as Péclet, Marangoni, and Stefan numbers, are employed to investigate advective transport in the meltpool for different alloys. Further, the framework is used to study variations in the thermal gradients and the solidification cooling rate. Important correlations linking meltpool morphology and microstructure-evolution-related variables with classical dimensionless numbers are the key contribution of this work.

Keywords: additive manufacturing; dimensionless numbers; finite element method; linear regression; cooling rates



Citation: Bhagat, K.; Rudraraju, S. A Numerical Investigation of Dimensionless Numbers Characterizing Meltpool Morphology of the Laser Powder Bed Fusion Process. *Materials* **2023**, *16*, 94. <https://doi.org/10.3390/ma16010094>

Academic Editor: Giulio Marchese

Received: 11 November 2022

Revised: 6 December 2022

Accepted: 15 December 2022

Published: 22 December 2022



Copyright: © 2022 by the authors. Licensee MDPI, Basel, Switzerland. This article is an open access article distributed under the terms and conditions of the Creative Commons Attribution (CC BY) license (<https://creativecommons.org/licenses/by/4.0/>).

1. Introduction

Additive manufacturing (AM) has proven to be a path-breaking manufacturing paradigm with the potential to disrupt many traditional reductive-type manufacturing processes [1]. A wide variety of AM techniques, suitable for printing metals, glasses, ceramics, and polymers [2], are in use today and an optimal AM technique can be selected depending on the material, part complexity and design considerations [3]. Laser Powder Bed Fusion (LPBF) AM process is the focus of this work. This technique is widely employed to print metallic components with intricate geometry to their near-net shape. Components printed using the LPBF process have the potential to exhibit improved material properties as compared to the traditional manufacturing process. In particular, additively manufactured hierarchical stainless steels are not limited by strength–ductility trade-off unlike traditionally manufactured stainless steel [4]. Tensile and fatigue properties of additively built Ti-6Al-4V were shown to be superior to mill-annealed Ti-6Al-4V [5]. However, the properties of the printed components are very sensitive to the LPBF process parameters selected and the execution of the printing process. Realizing the full potential of AM cannot

be achieved unless optimized process parameters can be identified for various alloys used in laser-based additive manufacturing [6].

The LPBF manufacturing technique is a multi-stage process. Initially, a moving blade of polymer edge (recoater) spreads a metal powder forming a layer of uniform thickness. A high-energy laser moves over a powder layer bed in a predefined path. This results in a localized melting of the powder metal followed by rapid cooling and fusion of melted-powder material on the previously built part. A new layer of the powder is then deposited and the process repeats until the desired part is printed in a layer-by-layer fashion [2]. This multi-stage additive printing process involves melting and solidification of the material, formation of the localized meltpool, convection cells inside the pool, keyhole formation, improper fusion of the powder, accumulation of residual stresses, and sometimes unwanted material deformation, etc. [7]. Existing literature is focused on understanding the effects of additive process parameters on the properties of experimentally printed components such as the surface roughness of overhang structures [8], bead geometry and microstructure [9], tensile strength [10], width and penetration depth of single scan track [11], etc. In addition to experimental studies, various LPBF processes, especially meltpool behavior [12], build layers [13], and laser heat source [14] effects have been analytically studied. Hybrid modeling that combines analytical models and machine-learning-based models is useful in estimating desirable meltpool dimensions and optimized process variables [15].

On the modeling front for LPBF, extensive literature has been published focused on the modeling of the rich multiphysics aspects of the process. Abolhasani et al. [16] studied the effect of reinforced materials on the cooling rates and meltpool behavior of AISI 304 stainless steel using finite element method simulations. Ansari et al. [17] developed a 3D finite-element method-based thermal model using a volumetric Gaussian laser heat source to model the thermal profile and meltpool size in selective laser melting process. The heat diffusion models were reinforced by considering localized dynamic and unsteady fluid flow inside the meltpool. Dong et al. [18] considered phase transformation, thermo-physical properties, heat transfer, and meltpool dynamics in their finite element model to investigate the effect of laser power and hatch spacing on the meltpool. A similar multiphysics model accounting for heat diffusion and fluid flow was presented by Ansari et al. [19] to study the effect of laser power and spot diameter on meltpool temperature in the LPBF process. Gusarov et al. [20] focused on heat transfer and radiation physics in their numerical model. More comprehensive numerical models of the LPBF consider temperature-dependent properties, powdered layer, fluid flow, laser scanning, etc. Mukherjee et al. [21] used comprehensive LPBF numerical models to simulate fluid flow and heat diffusion dynamics for most commonly used alloys. Khairallah et al. [22] provided richer insights into LPBF printing of stainless steel using various continuum numerical models. Wang et al. [23] coupled finite volume, discrete element, and volume of fluid methods to rigorously model power spreading, powder melting, and multi-layer effects during LPBF AM of Ti-6Al-4V alloy. In trying to capture all the important aspects of the LPBF process in a numerical model, challenges exist in terms of numerous variables, process parameters, and their complex interactions, and these are outlined in the work of Keshavarzkermani et al. [24] and Fayazfar et al. [25].

Physical processes involving many independent parameters can be analyzed and investigated using dimensional analysis. Traditional areas of physics and engineering, especially fluid mechanics and heat transfer have used dimensional and scaling analysis extensively [26]. Researchers in AM-related problems have recently started incorporating dimensional analysis in their work. Van Elsen et al. [27] provided a comprehensive list of dimensionless quantities that are relevant for the additive and rapid manufacturing process. They justified the usability of the dimensional analysis to investigate complex additive processes such as LPBF. Dimensionless numbers were shown to assist in choosing previously unknown process parameters for the LPBF process to print Haynes 282, a nickel-based superalloy [28]. Weaver et al. [29] demonstrated the application of universal scaling laws to study the effect of process variables such as laser spot radius on the meltpool depth.

Rankouhi et al. [30] in their experimental work applied the Buckingham- π theorem in conjunction with Pawlowski matrix transformation to present dimensionless quantities that correlate well with the density or porosity of the built component. Their proposed non-dimensional quantity is shown to be applicable across different material properties and machine variables, thereby achieving desirable scaling. Another widely applicable dimensionless quantity, referred to as Keyhole number, was proposed by Gan et al. [31]. They made use of dimensionless analysis in conjunction with multiphysics numerical models and high-tech X-ray imaging in their discovery. Keyhole number provides useful insights into the aspect ratio of the meltpool and the transformation of the meltpool from a stable to a chaotic regime. Wang and Liu [32] proposed four sets of dimensionless quantities combining process parameters and material properties. Their experimental analysis shows that these numbers can effectively characterize phenomena such as the continuity of the track and its size and the part porosity. Noh et al. [33] showed that normalized enthalpy and relative penetration depth in the vertical direction can provide reliable process map for printing single-track 3D geometries using selective laser melting process.

The published literature surveyed for this work either uses experimental or numerical methods to propose new dimensionless quantities that are specific to the AM process and are not always related to classical dimensionless numbers used in the fields of fluid mechanics and heat transfer. Classical dimensionless numbers such as the Péclet number can provide a good understanding of the impact of process variables on the printed components. Nusselt, Fourier, and Marangoni numbers provide a good understanding of the mode of heat transport inside the meltpool for varying laser power and scan speed [34,35]. Cardaropoli et al. [36] provided a map for Ti-6Al-4V alloy linking dimensionless quantities with the porosity of built parts. Mukherjee et al. [37] used their established numerical models of the LPBF process to simulate the building of different materials with varied process variables. Using a known set of dimensionless numbers representing heat input, Péclet, Marangoni, and Fourier numbers, they made sense of the impact of process parameters on important output variables such as temperature field, cooling rates, fusion defects, etc.

Similar to the meltpool in the LPBF process, the traditional welding process also involves the formation of a weldpool which is the site of various multiphysics interactions and processes. Literature on the use of dimensional analysis to understand the flow patterns in the weldpool offers relevant insights to AM. This includes work by Robert and Debroy [38] where they highlighted the importance of dimensionless numbers such as Prandtl, Péclet, and Marangoni in understanding the aspect ratio of the weldpool. Using the numerical models to predict the weldpool shape for a range of materials, they presented the insightful role of these numbers in shaping the weldpool morphology. Similarly, Lu et al. [39] also discuss the role of Marangoni convection in affecting the aspect ratio and shape of the weldpool. Their analysis shows that the effect of welding process conditions on the weld part can be understood by analyzing the non-dimensional numbers such as Péclet and Marangoni. Wei et al. [40] showed that the formation of a wavy fusion boundary is linked with the critical values of the Marangoni and Prandtl numbers. Fusion boundaries and shapes have a significant impact on the microstructure of the material. Asztalos et al. [41] applied dimensional analysis to study the polymer additive manufacturing processes.

As can be seen from the literature review presented, the use of dimensionless numbers to understand the complex interaction of physical processes is gaining attention. However, among the proposed dimensionless quantities, few are universally applicable. Some of them remain applicable only in the context of a specific study or alloy. A universal dimensionless variable or normalized graph can facilitate the comparison of results between different studies using different materials [42]. This leaves room for the development of novel approaches to characterize the LPBF process using dimensional analysis. Our goal in this work is to perform such a dimensional analysis and investigate the relation between meltpool morphology and to a lesser degree, microstructure evolution, and the underlying dimensionless quantities naturally manifested by the thermo-fluidic governing equations of the LPBF process. In this context, a novel numerical strategy is herein presented, where

the data generated using numerical simulations of the thermo-fluidic model for different alloys and different process parameters were used, along with linear regression analysis, to characterize meltpool morphology in terms of the dimensionless numbers relevant to the meltpool heat and mass transport.

The outline of the paper is as follows: Section 2 introduces the governing equations of the LPBF process in their dimensional and non-dimensional forms, along with the corresponding numerical formulation suitable to be solved using the Finite Element (FE) method. Section 3 covers the validation of our FE-based implementation of the LPBF thermo-fluidic model with experimental results and numerical results from the literature. In Section 4, an empirical analysis based on linear least-squares regression is described to identify an important dimensionless quantity that is interpreted as a measure of heat absorbed by the powdered material and the resulting meltpool. An important relationship is then identified relating the measure of heat absorbed by the meltpool and classical dimensionless quantities relevant to the thermo-fluidic governing equations of the LPBF. This is followed by a presentation of simulation results in Section 5, including a discussion on the effects of the dimensionless quantities on the meltpool morphology and the resulting microstructure. Lastly, concluding remarks are provided in Section 6.

2. Governing Equations of the LPBF Process

2.1. Thermo-Fluidic Model of the LPBF Process

A discussion of the physical processes underlying LPBF that are relevant to the thermo-fluidic model is outlined in this section. The schematic in Figure 1 shows an outline of the LPBF process. In LPBF, a recoater spreads a metal-powder layer on top of the powder bed or partially built part that is enclosed in an inert environment. A high-intensity laser scans over this powder layer, causing localized melting and fusion of the melted powder on top of the partially built part. At the macro-scale or part-scale, this laser irradiation of the metal powder results in the formation of a *meltpool* (also referred to as *molten pool* or *melting pool* in the literature) of the liquified metal, that subsequently solidifies. This solidification of the meltpool is driven from the mesoscale, where the liquid melt undergoes a phase transformation to a solid phase, but the solidification is spatially heterogeneous and leads to the formation of dendritic structures and eventually the grain-scale microstructure. The formation of dendrites, their morphology, and the related numerical models were extensively investigated by the authors in a recent publication [43].

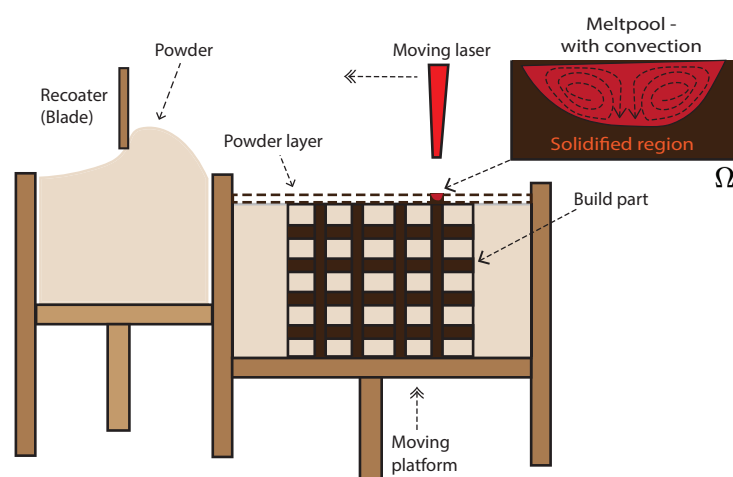


Figure 1. Schematic depicting the part-building process in Laser Powder Bed Fusion (LPBF). Laser irradiation on the powdered material causes localized melting and fusion of the metal powder on top of the partially built part. The localized melting results in a small pool of liquified metal referred to as the *meltpool*. Shown in the inset figure are the state of the powder under the laser—with the newly solidified region and a meltpool with convective flow of the liquified metal, and this region comprises the computational domain (Ω) of the numerical model presented in this work.

In this work, the part-scale and thermo-fluidic processes that are relevant in the meltpool and its immediate vicinity are considered. The processes modeled, with varying fidelity, include the movement of the laser-powered heat source, powder melting, convective flow in the meltpool, heat diffusion, and convective and radiation losses. These processes and their thermo-fluidic effects can be captured by coupled partial differential equations solving for the thermal distribution and the velocity distribution in the meltpool [21].

The governing equations of heat transfer are as follows:

$$\rho c \frac{\partial T(\mathbf{x}, t)}{\partial t} + \rho(\mathbf{v} \cdot \nabla)T(\mathbf{x}, t) = \nabla \cdot \mathbf{k}(\nabla T(\mathbf{x}, t)) + S_\phi + S_p, \quad \mathbf{x} \in \Omega \quad (1)$$

Equation (1) is solved for thermal conduction over the domain Ω (see Figure 1). T and \mathbf{v} are the temperature and velocity, respectively, and are the primal fields of the governing equations. All through this work, vector quantities such as velocity and the gradient operator, ∇ , are shown in bold to distinguish them from other scalar quantities.

S_p is the heat input from the laser and S_ϕ is the latent heat released by the metal. ρ , c , k represent density, specific heat capacity, and the thermal conductivity of the material, respectively, and these can be constant or temperature dependent. Melting of the metal powder consumes latent heat, which is represented by source term, $S_\phi = -\rho(\mathbf{v} \cdot \nabla)\phi - \rho L(\frac{\partial \phi}{\partial t})$. Here the liquid fraction, ϕ , determines the state of the material. $\phi = 0$ represents the solidified region, $\phi = 1$ represents the liquid, and $0 < \phi < 1$ represents the mushy zone region [44]. The liquid fraction is a function of the temperature of the material and is given by the hyperbolic function: $\phi = \frac{e^\xi}{e^\xi + e^{-\xi}}$, where $\xi = \frac{\lambda(T - T_m)}{T_l - T_s}$ and $T_m = \frac{1}{2}(T_l + T_s)$. λ is a constant that represents the solid-liquid interface thickness, T_s , and T_l are the solidus and the liquidus temperature of the material, respectively. The shape of the laser beam is modeled as an axisymmetric Gaussian profile, and the moving laser power is modeled using a source term, $S_p = \frac{\alpha f P}{\pi r_p^2 l_p} e^{-\frac{f(x - v_p t)^2}{r_p^2} - \frac{f y^2}{r_p^2} - \frac{f z^2}{l_p^2}}$, where P is the laser power, α is the absorptivity, f is the distribution factor, r_p is the laser spot size, l_p is the powder layer thickness, and v_p is the laser scan speed.

Effectively, thermal conduction, powder melting due to the moving laser, and the formation of a liquid meltpool are modeled. Inside the meltpool, heat diffusion, along with the advection and convection effects of the fluid flow are considered. Convection inside the meltpool is a result of the competition between the surface tension and the buoyancy effects, but the surface tension driven flow dominates inside the meltpool [45]. The governing equations for the fluid flow, accounting for the conservation of mass and momentum, are given by,

$$\rho \frac{\partial \mathbf{v}(\mathbf{x}, t)}{\partial t} + \rho(\mathbf{v}(\mathbf{x}, t) \cdot \nabla)\mathbf{v}(\mathbf{x}, t) = -\nabla p + \beta g(T - T_s) + \nabla \cdot (\mu \nabla \mathbf{v}(\mathbf{x}, t)) - \frac{180\mu(1 - \phi)^2}{d_\phi^2 \phi^3 + \delta} \mathbf{v}(\mathbf{x}, t) \quad (2)$$

$$\nabla \cdot \mathbf{v}(\mathbf{x}, t) = 0, \quad \mathbf{x} \in \Omega \quad (3)$$

This equation also accounts for advective and diffusive transport, buoyancy-induced flow, and the pressure drop due to the mushy zone (modeled as a porous zone) [44]. Here, β is the expansion coefficient, T_s is the solidus temperature, μ is the dynamic viscosity, d_ϕ is the characteristic length scale of the porous mushy region, and δ is a very small parameter to avoid division by zero when $\phi = 0$ (solid region). Integral form of governing equations introduced in Section 2.2 are given by Equations (4) and (5). As will be seen in the integral form, the surface integrals therein also account for the surface tension-induced flow and losses to the inert surroundings. This is captured by the inclusion of the convective and radiation heat losses, Marangoni convection from the top surface of the domain, Ω . At the bottom surface, temperature is fixed to a preheating temperature value that is above the ambient temperature. To limit the modeling complexity, in this otherwise highly coupled multiphysics environment, mechanical deformation of the solidified region and keyhole formation is neglected.

2.2. Non-Dimensional Formulation of the Governing Equations

In this section, a dimensionless framework is constructed that exploits the powerful idea of the Buckingham- π theorem. The LPBF process consists of several process parameters and the thermo-fluidic model that helps us build an understanding of the complex interaction between several of these process parameters. The dimensionless framework facilitates combining several of these dimensional parameters into fewer dimensionless independent quantities. These dimensionless parameters then present key details of the complex additive process such as LPBF in fewer numbers of variables. The classical Buckingham- π theorem [46] provides a mathematical basis for reducing the parameter dimensionality of the equations and helps group the parameters in the governing equations into a fewer number of non-dimensional and distinct quantities. This reduction follows from the application of the Rank-Nullity theorem [47,48]. Further, as will be discussed in later sections, the Finite Element Method (FEM) is employed to solve the governing equations considered in this work. FEM is a widely used numerical method that solves partial differential equations posed in their weak formulation (integral formulation). Thus, the dimensionless version of the governing equations that results from the application of the Buckingham- π theorem is also considered in its weak form and solved using FEM.

Weak Formulation

In this section, the process of non-dimensionalization of the governing equations given by Equations (1)–(3) is discussed. For the process of non-dimensionalization, the laser scan velocity, v_p is chosen as the characteristic velocity in the system, and the non-dimensional velocity in the meltpool is then given by $\tilde{v} = \frac{v}{v_p}$. The thickness of the powder layer, l_p , is chosen as the characteristic length, and this leads to the characteristic time, given by $t_p = \frac{l_p}{v_p}$. Now, the non-dimensional time and length are given by $\tilde{t} = \frac{t}{t_p}$ and $\tilde{x} = \frac{x}{l_p}$, respectively. Further, the non-dimensional temperature is chosen to be $\tilde{T} = \frac{T - T_\infty}{T_l - T_\infty}$, where T_l and T_∞ are the liquidus temperature of the metal and the ambient temperature of the inert surroundings, respectively. The characteristic value of the pressure is chosen to be ρv_p^2 . A list of the dimensionless variables used in this model are summarized in Table 1. Using these scaled quantities, the dimensional strong (differential) form of the governing equations given by Equations (1)–(3) are converted into their corresponding dimensionless weak (integral) form. Following the standard variational procedure of deriving the weak formulation of the governing equations from their strong form [49], the following weak formulation is obtained:

Find the primal fields, $\{\tilde{T}, \tilde{v}\}$, where,

$$\begin{aligned}\tilde{T} \in \mathcal{S}_T, \quad \mathcal{S}_T &= \{\tilde{T} \in H^1(\Omega) \mid \tilde{T} = \tilde{T}' \forall \mathbf{x} \in \partial\Omega_D^T\}, \\ \tilde{v} \in \mathcal{S}_v, \quad \mathcal{S}_v &= \{\tilde{v} \in H^1(\Omega) \mid \tilde{v} = \tilde{v}' \forall \mathbf{x} \in \partial\Omega_D^v\}\end{aligned}$$

such that,

$$\begin{aligned}\forall \omega_T \in \mathcal{Y}_u, \quad \mathcal{Y}_T &= \{\omega_T \in H^1(\Omega) \mid \omega_T = 0 \forall \mathbf{x} \in \partial\Omega_D^T\}, \\ \forall \omega_v \in \mathcal{Y}_\phi, \quad \mathcal{Y}_\phi &= \{\omega_v \in H^1(\Omega) \mid \omega_v = 0 \forall \mathbf{x} \in \partial\Omega_D^v\}\end{aligned}$$

and satisfies,

$$\begin{aligned}\int_{\Omega} \omega_T \left(\frac{\partial \tilde{T}}{\partial \tilde{t}} + (\tilde{v} \cdot \tilde{\nabla}) \tilde{T} \right) d\Omega + \int_{\Omega} \nabla \omega_T \cdot \left[\frac{1}{Pe} \right] \tilde{\nabla} \tilde{T} d\Omega + \int_{\Omega} \omega_T \left[\frac{Tc}{Ste} \right] \left((\tilde{v} \cdot \tilde{\nabla}) \tilde{\phi} + \frac{\partial \tilde{\phi}}{\partial \tilde{t}} \right) d\Omega \\ - \int_{\Omega} \omega_T \frac{\alpha f}{\pi \tilde{r}^2 \tilde{l}} [\mathbf{Q}] \exp(\tilde{x}, \tilde{y}, \tilde{z}) d\Omega + \int_{\partial\Omega_N^T} \omega_T \left(\left[\frac{Bi}{Pe} \right] \tilde{T} + \left[\frac{ts}{Bo} \right] \tilde{T} \right) n dS = 0\end{aligned}\quad (4)$$

$$\int_{\Omega} \omega_v \left(\frac{\partial \tilde{v}}{\partial \tilde{t}} + \tilde{v} \cdot \tilde{\nabla} \tilde{v} \right) d\Omega - \int_{\Omega} \omega_v \left[\frac{RaPr}{Pe^2} \right] (\tilde{T} - \tilde{T}_s) d\Omega - \int_{\Omega} \tilde{\nabla} \cdot \omega_v \tilde{p} d\Omega + \int_{\Omega} \omega_v \left[\frac{Pr}{DaPe} \right] \tilde{v} d\Omega + \int_{\Omega} \left[\frac{Pr}{Pe} \right] (\tilde{\nabla} \omega_v \cdot \tilde{\nabla} \tilde{v}) d\Omega + \int_{\partial\Omega_N^v} \omega_v \left(\tilde{p} - \left[\frac{MaPr}{Pe^2} \right] \tilde{\nabla} \tilde{T} \right) \mathbf{n} dS = 0 \quad (5)$$

here, \mathbf{n} is the unit outward normal vector at the surface boundary. $\partial\Omega_N^T$ and $\partial\Omega_N^v$ are the boundaries for the temperature and velocity Neumann boundary conditions, respectively, and $\partial\Omega_D^T$ and $\partial\Omega_D^v$ are the boundaries for the temperature and velocity Dirichlet boundary conditions, respectively. ω_T and ω_v are standard variations from the space $H^1(\Omega)$ —the Sobolev space of functions that are square-integrable and have a square-integrable derivatives. In these equations, the relevant dimensionless numbers are grouped inside square brackets. These dimensionless numbers, along with their physical interpretation, are listed in Table 2. The surface boundary condition in Equation (4) represents the nondimensional form of the convective and radiation heat losses to the inert surrounding, and the boundary condition (on the top surface) in Equation (5) represents the Marangoni flow induced by the surface tension gradient.

Table 1. List of the scaling variables used in the non-dimensionalization of Equations (4) and (5).

Parameter	Expression	Physical Interpretation
\tilde{l}	$\frac{l_p}{l_p}$	Dimensionless powder layer thickness
\tilde{r}	$\frac{r_s}{l_p}$	Dimensionless laser spot radius
\tilde{t}	$\frac{t v_p}{l_p}$	Dimensionless time
\tilde{T}	$\frac{T - T_{\infty}}{T_l - T_{\infty}}$	Dimensionless temperature
\tilde{v}	$\frac{v}{v_p}$	Dimensionless velocity
\tilde{p}	$\frac{p}{\rho v_p^2}$	Dimensionless pressure
$\tilde{\nabla}$	$\frac{1}{l_p} \nabla$	Dimensionless gradient operator

Table 2. Symbols, expressions and their physical interpretation for the dimensionless quantities considered in Equations (4) and (5).

Parameter	Expression	Physical Interpretation
Prandtl (Pr)	$\frac{\nu}{\alpha}$	Ratio of momentum to thermal diffusivity
Grashof (Gr)	$\frac{g \beta (T_l - T_{\infty}) l_p^3}{\nu^2}$	Ratio of buoyancy force to viscous force
Darcy (Da)	$\frac{k}{d_p^2}$	Ratio of permeability to the cross-sectional area
Marangoni (Ma)	$\frac{d\gamma}{dT} \frac{l_p \Delta T}{\mu \alpha}$	Ratio of advection (surface tension) to diffusive transport
Péclet (Pe)	$\frac{l_p v_p}{\alpha}$	Ratio of advection transport to diffusive transport
Stefan (Ste)	$\frac{c(T_l - T_s)}{b}$	Ratio of sensible heat to latent heat
Power (Q)	$\frac{\rho c (T_l - T_{\infty}) v_p l_p^2}{b}$	Dimensionless power with velocity dependence
Radiation measure ($\frac{I_s}{Bo}$)	$\frac{\sigma (T_l - T_{\infty})^3}{\rho c v_p}$	Measure of radiation contribution to the heat transfer
Biot (Bi)	$\frac{h l_p}{k}$	Ratio of resistance to diffusion and convection heat transport

2.3. Computational Implementation

As stated earlier, the above weak formulation of the governing equations is solved using FEM, and as model inputs, realistic process parameters and material properties of common LPBF alloys are chosen, and these are discussed in Section 4.1 and in the Supplementary Information. FEM implementation is done in an in-house, scalable, finite element code framework written in C++ language with support for adaptive meshing and various implicit and explicit time-stepping schemes, and is built on top of the deal.II open-source Finite Element library [50]. Standard FEM constructs are adopted, and for all simulations presented in this work, linear and quadratic Lagrange bases are used for pressure and other field variables such as temperature and velocity, respectively. The coupled Navier–Stokes equations are solved using Chorin’s projection method [51]. Following the standard practice in our group to release all research codes as open source [43,52–55], the complete code

base for this work is made available to the wider research community as an open-source library [56]. A representative schematic of the computational domain and the relevant boundary conditions are shown in Figure 2. The important boundary conditions such as convective and radiations losses and shear stress on the top surface expressed as surface tension gradient with temperature is visible in the surface integral terms in Equations (4) and (5). The initial temperature and temperature at the bottom surface of the material are assumed to be fixed at 353 K. The ambient temperature was taken as 301.15 K. These temperatures were scaled to a dimensionless form in the computational implementation. The minimum and maximum dimensionless mesh sizes in an adaptive meshing scheme are taken to be $\Delta x = 0.8$ and $\Delta x = 6.0$ along the x , y , and z directions. A uniform dimensionless time step size of $\Delta t = 1.0$ is used for running test cases. The small factor in Equation (2), $\delta = 1.0 \times 10^{-5}$ is used in all the simulations. The interface parameter (λ) used in our simulation is in the range $\lambda = [0.1, 1.0]$.

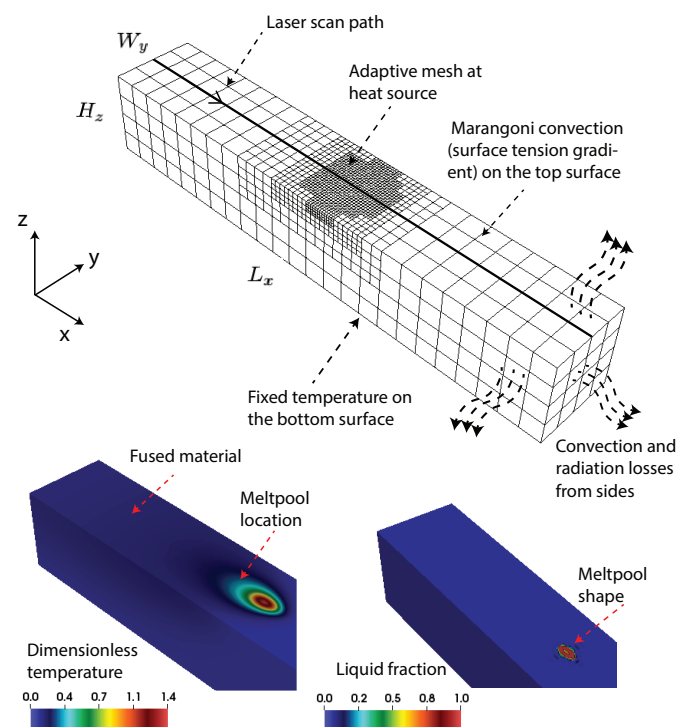


Figure 2. Schematic of the 3D finite element (FE) computational domain indicating the laser scan path and the relevant boundary conditions. Shown also is the underlying adaptive mesh that evolves with the location of the heat source. Representative dimensionless temperature profile and location of the meltpool obtained from the FE simulation of SS316 alloy AM are shown. The numerical parameters and material properties used in this simulation are given in Section 2.3 and in the Supplementary Information.

3. Experimental and Numerical Validation

In this section, a validation of the numerical formulation and the FEM-based computational framework is presented. This computational framework solves the thermo-fluidic governing equations of the meltpool described in Section 2. Further, a comparison is given between the simulation results with experimentally observed cooling rates (made available to us by our experimental collaborators), and with predictions of other numerical models from the literature. Variables such as the cooling rates during the solidification, material temperature, velocity of fluid inside the pool, and meltpool geometry can be used as a yardstick to gauge the capability of our numerical model towards simulating the LPBF process. For this validation study, the temperature and velocity distributions, the cooling rates, and the maximum velocity in the meltpool are obtained from our FEM

implementation. The cooling rate estimates from our simulations are compared with the cooling rates estimated from experimental data of the LPBF process that were obtained from Bertsch et al. [57]. Further, our simulation results are compared with the corresponding material temperature distribution and meltpool velocity values obtained from numerical modeling data in Shen et al. [58]. Simple thin-walled pseudo-2D plates and 3D cuboidal geometries made of stainless steel (SS316 alloy) using the LPBF process are considered in this validation study. The printed geometries consists of $13 \times 0.2 \times 13 \text{ mm}^3$ thin wall plates and $50 \times 10 \times 4 \text{ mm}^3$ cuboids. The schematic of the printed 2D plates and 3D cuboidal geometries can be found in Bertsch et al. [57]. These geometries are subsequently referred to as the 2D walls and 3D cuboids. The powder layer thickness used was 0.02 mm in both cases. Experimental details, AM technical specifications, and the post-processing methods used to measure cooling rates can be found in the publications of our experimental collaborators, Bertsch et al. [57] and Rankouhi et al. [59]. The experimental cooling rates were estimated by our collaborators, through post-processing of the microstructure morphology, particularly the secondary dendrite arm spacing (λ_2) at a distance of 6.5 mm and 2 mm from the base for the 2D walls and 3D cuboids, respectively. The dendritic arm spacing in the printed parts was analyzed by our collaborators using a scanning electron microscope (SEM) following standard post-processing techniques. The cooling rates for the alloy SS316 were obtained using the relation $\lambda_2 = 25\dot{\epsilon}^{-0.28}$ [60], where λ_2 is measured from SEM images.

For obtaining the numerical results, temperature-dependent material properties of the SS316 stainless steel alloy are considered separately for the powdered, fused, and liquid state of the material. The temperature and velocity distributions inside the meltpool were obtained from the FE model. The cooling rates are given by the expression $|\nabla T|v_p$, where $|\nabla T|_2$ is a measure of the average temperature gradient in the meltpool, and v_p is the laser scanning speed. For the 2D plates, the cooling rate was measured at a location 6.5 mm from the base, both in the experiments and the FE model. Similarly, for the 3D cuboids, cooling rate estimates were obtained at a location 2 mm from the base, both in the experiments and the FE model. As can be seen from Figure 3, the cooling rates obtained from the FE model are close to the experimentally reported values. The cooling rates are used for comparison with experiments in this work, as they are of immense practical interest due to their influence over the evolution of the microstructure (dendritic growth and grain growth) that then dictates the mechanical properties of the printed part.

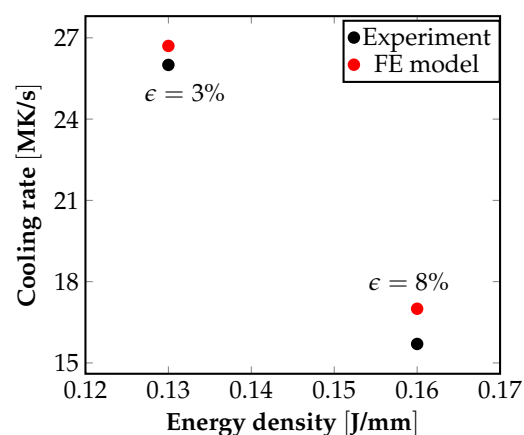


Figure 3. Dependence of cooling rates obtained from experiments and the FE model on the energy density, $\frac{P}{v_p}$. The average cooling rate from the FE model was estimated using the relation: $\dot{T} = Gv_p = |\nabla T|v_p$. Laser power (W) and scan speed (mm/s) combinations used for this study were $(P, v_p) = (90, 575), (90, 675)$.

Further, the temperature distribution and maximum velocity values in the meltpool obtained from the FE model were compared against the reference test cases given in Shen et al. [58]. These cases represent the simulation of an LPBF process with a laser power

of 100W and 200W used to print AZ91D magnesium alloy parts. As shown in Figure 4a–c, the point temperature as a function of time and the maximum meltpool velocity values obtained from our numerical model closely matches the trend reported in the literature. These comparisons provide a good validation of our FE-based numerical formulation and its computational implementation.

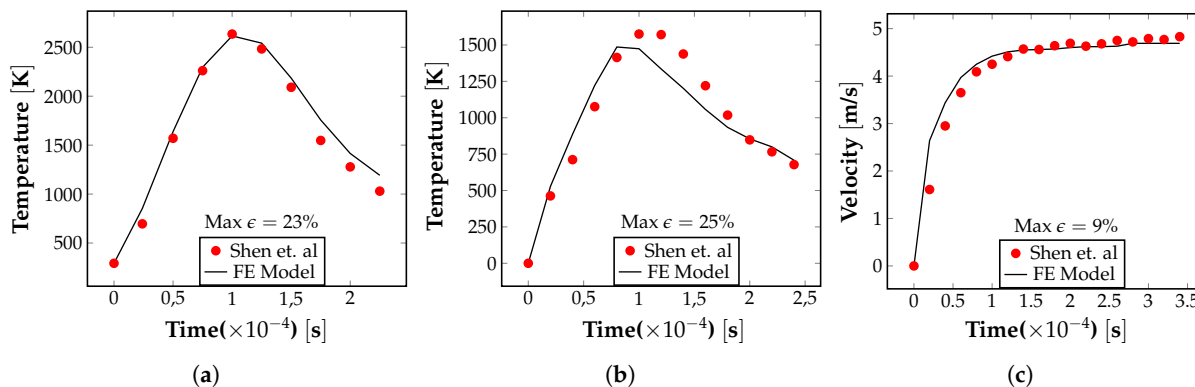


Figure 4. Validation of the FE model results by comparing with corresponding values reported in the literature. (a) Variation in point temperature with time for the case P = 200 W. (b) Variation in point temperature with time for the case P = 100 W. (c) Variation in maximum pool velocity with time for the case P = 100 W [58].

4. Empirical Analysis of the Energy Absorbed by the Meltpool

In this section, the rationale behind the construction of a model of the energy absorbed by the meltpool is discussed. Numerical modeling of the AM process, in general, solves governing equations of heat conduction, fluid flow, mechanical deformation of the solidified region, etc., that is in terms of “local” field quantities such as temperature, velocity, displacement, etc. However, our goal in this work is to arrive at estimates of the “global” response of the system at the meltpool-scale, i.e., measures such as the meltpool morphology (size and shape), average temperature distribution, average velocity distribution, etc. *The intention is to propose and validate a “global” model of the energy absorbed by the meltpool in terms of various process variables, material properties, and output variables, and thus determine the important quantities, from amongst these dependencies, that have the most direct impact on meltpool evolution.*

Towards proposing a linear model of the heat energy absorbed by the meltpool, various non-dimensional quantities are chosen that appear in Equations (4) and (5). These are the input quantities made up of material properties, processing conditions, and surrounding environment variables. The general procedure used to estimate a linear model is as follows: \hat{U} , the dimensionless measure of the heat absorbed by the meltpool, and modeled as linearly dependent on the input non-dimensional quantities. Such a model can be mathematically expressed as $\hat{U} = \sum_{i=0}^n a_i \pi_i$, where n , π_i , and a_i denote the number of inputs, the dimensionless numbers considered and their corresponding coefficients, respectively. The merits and demerits of choosing various input non-dimensional quantities to characterize the model are evaluated using physics-based and statistical arguments discussed in the subsequent sections. Broadly, a method of least squares numerical approach is implemented to estimate the coefficients, a_i , corresponding to each dimensionless number, π_i , considered as a potential variable influencing the heat absorbed by the meltpool. It is the relative magnitude of these coefficients that inform us about the significance or insignificance of each dimensionless quantity towards the model of the heat absorbed. Further, it is understood from prior knowledge that a system with higher \hat{U} can potentially correlate to a rise in some measure of the meltpool temperature. The maximum temperature of the material is arguably higher if the heat received \hat{U} is higher. Thus, as a first-order argument, there exists a phenomenological relation $\hat{U} \propto \tilde{T}_{max}$. This reasoning permits us to use \tilde{T}_{max} as a measure of the \hat{U} , and the value of \tilde{T}_{max} is obtained by solving thermo-fluidic model

described by Equations (4) and (5) on different alloy materials and processing conditions listed in the Tables S1 and S2 provided in the Supplementary Information. Having obtained \tilde{T}_{max} , the coefficients, a_i are estimated, using the method of linear least squares approach and an explicit form \hat{U} in terms of various dimensionless numbers, π_i is obtained. Once the linear model of the heat absorbed by the meltpool, \hat{U} , is determined, it is linked with the several output variables of interest, namely the temperature gradient in the meltpool, the solidification cooling rate (Gv_p), a measure of the advection heat transport due to the surface tension gradient, and finally the meltpool morphology (aspect ratio ($\frac{l_m}{w_m}$) and volume ($l_m w_m d_m$)). Important correlations between the relevant output variables and nondimensional input numbers are discussed at length in Section 5.

4.1. Process Variables, Material Properties, and Output Variables

In this section, the process variables such as laser characteristics, the material properties of the alloy, and the output variables obtained from the thermo-fluidic model are discussed. The powder layer thickness $l_p = 0.02$ mm and laser spot radius $r_p = 0.1$ mm are taken for all the cases. The simulation domain geometry, $L_x \times W_y \times H_z = 3 \times 0.5 \times 0.5$ mm³, is fixed for all the cases. The movement of the laser is modeled as a single scan on the centerline of the top surface. The temporal and 3D spatial variations of the temperature and velocity of the material in the meltpool are obtained from the FE model. Due to the laser heat source, the temperature of the material increases past the liquidus melting temperature and results in the formation of a liquid meltpool. In the simulations, five commonly used LPBF alloy materials are considered, namely stainless steel (SS316), a Titanium alloy (Ti-6Al-4V), a Nickel Alloy (Inconel 718), an Aluminium alloy (AlSi10Mg), and a Magnesium alloy (AZ91D) [21,22,58]. To limit the complexity of the analysis by making dimensionless quantities independent of temperature, constant material properties (non-varying with temperature) are chosen. The numerical values of the input material properties for each of the alloys considered are provided in the Supplementary Information.

The process variables considered are the laser power value (P) and laser scan speed v_p , a laser distribution factor, $f = 2.0$, is fixed for all the cases. For a given alloy, twelve (4×3) combinations of the process variables were chosen to simulate a range of process conditions that are relevant to the LPBF process. The numerical values of the input process properties for each of the alloys considered are provided in the Supplementary Information, under Tables S1 and S2. In the thermo-fluidic model, the heat transfer coefficient (h) and the Stefan-Boltzmann constant (σ) are associated with the surrounding inert environment. $\sigma = 5.67 \times 10^{-8}$ W/(m²K⁴) is a known constant. The effect of varying the heat transfer coefficient is found to have a negligible impact based on our preliminary simulations, so the heat transfer coefficient is taken as $h = 10$ W/m²K. This is due to the relatively minimal convective and radiation losses to the environment, as compared to conduction of heat through the base plate. In total, we perform about 60 ($5 \times 4 \times 3$) LPBF simulations considering different process variables and material properties. At a fixed non-dimensional time $\tilde{t} = 100$, the maximum value of the magnitude of the temperature gradient $G = |\nabla T|$ is recorded. The temperature gradient value in the meltpool region is significant but relatively small outside this region. The temperature gradient is an important variable that controls the microstructure evolution in the additively printed material. The cooling rate, given by Gv_p , where v_p is the speed of the solid-liquid interface is also an important output variable for understanding the microstructure evolution. Further, the maximum temperature, T_{max} , and maximum velocity, v_{max} , in the meltpool, is tracked along with a measure of the maximum extent of the meltpool length (l_m), width (w_m) and depth (d_m) that characterize the meltpool morphology.

4.2. Parametrization in Terms of the Dimensionless Quantities

The use of an empirical approach to estimate \hat{U} is described in this section. The most appropriate set of dimensionless input parameters that explain variation in the measure of the heat absorbed is chosen. As stated earlier, \hat{U} is considered proportional to \tilde{T}_{max} .

In total, 60 correlations of the form (Π, \tilde{T}_{max}) are generated from our simulations, where Π represents the set of the dimensionless input quantities considered. The unknown coefficients, (a_i) are determined through the standard method of linear least-squares regression. The data for the regression analysis are obtained from the finite element simulations of the LPBF process. Here, multiple regression attempts were made to arrive at a linear characterization of \hat{U} in terms of the most relevant dimensionless input quantities. While many combinations of the dimensionless input quantities were considered, three such attempts as representative of our regression analysis are presented here. The first two attempts result in correlations that are weak and hence discarded, before converging onto an acceptable correlation between \hat{U} and the relevant dimensionless input quantities in the third attempt.

First attempt of the regression analysis:

The following set of independent variables: $\Pi = \{ \frac{1}{Pe}, Q, \frac{Tc}{Ste}, \frac{Bi}{Pe}, \frac{ts}{Bo} \}$ are considered. The hypothesized linear relationship is shown below. Here ϵ is the error—the difference between the expected and true value of \hat{U} .

$$\hat{U} = a_0 + a_1 Q + a_2 Pe^{-1} + a_3 \frac{Tc}{Ste} + a_4 \frac{Bi}{Pe} + a_5 \frac{ts}{Bo} + \epsilon \tag{6}$$

The values of the coefficients resulting from the least-squares regression are given in Table 3. The condition number for this analysis is 8.11×10^7 , which is very high. This indicates that there exists strong collinearity in the assumed input set Π . The collinearity can be understood in terms of the primary variable as follows: On close inspection of the dimensionless expressions for $Q = \frac{P}{\rho c(T_1 - T_\infty) v_p l_p^2}$, $\frac{1}{Pe} = \frac{\alpha}{v_p l_p}$, $\frac{Bi}{Pe} = \frac{hl\alpha}{v_p l_p}$, and $\frac{ts}{Bo} = \frac{\sigma(T_1 - T_\infty)^3}{\rho c v_p}$, it is observed that laser scan velocity is accounted for in all the four variables, and this can potentially reduce the linear independence of these physical quantities. Further, the role of inert environment variables is limited in our analysis. Considering the regression coefficients, Bi/Pe and ts/Bo are dropped from our next regression attempt.

Table 3. First attempt of the regression analysis to estimate the coefficients, a_i , using the linear least-squares approach. Asterisk (*) indicates the statistical significance of the coefficient using a t-test with a 95% confidence interval. Other statistics: $R^2 = 0.65$, Adjusted $R^2 = 0.61$, F-statistic = 20.12, P(F) = 0.0. Condition number = 8.11×10^7 .

Parameter	Intercept	Q	Pe ⁻¹	$\frac{Tc}{Ste}$	$\frac{Bi}{Pe}$	$\frac{ts}{Bo}$
a_i	1.45 *	0.0053 *	-0.1719 *	-0.7076 *	300.3	-18,200 *

Second attempt of the regression analysis:

In the second iteration, the chosen independent set is $\Pi = \{ E, Pe, \frac{Tc}{Ste} \}$. The hypothesized linear relationship is given by the following relation.

$$\hat{U} = a_0 + a_1 E + a_2 Pe + a_3 \frac{Tc}{Ste} + \epsilon \tag{7}$$

Further, considering the details of the regression analysis, the expression for the variable dimensionless power, Q , that had a velocity dependence is modified to a new variable, $E = \frac{P}{k(T_1 - T_\infty)} = PeQ$. This new variable is a modified dimensionless power and is independent of the laser scan velocity. Now, the laser scan speed parameter is only represented in the Péclet number, Pe . The fourth term $\frac{Tc}{Ste}$ is purely dependent on the material properties. Note the least-squares solution yields the coefficients given in Table 4.

The least-square solution obtained from this model is an improvement over the previous model. This can be realized from the improvement in the accuracy of the fit given by the variable R^2 . The adjusted R^2 improves from 0.65 to 0.75 with the less number of

variables in the set Π . The condition number is still high but better than the previous model. Thus, the non-significant variable is dropped from the set, Π , in our third attempt.

Table 4. Second attempt of the regression analysis to estimate the coefficients, a_i , using the linear least-squares approach. Asterisk (*) indicates the statistical significance of the coefficient using a t-test with a 95% confidence interval. Other statistics: $R^2 = 0.763$, Adjusted $R^2 = 0.750$, F-statistic = 55.95, $P(F) = 0.0$. Condition number = 1.12×10^3 .

Parameter	Intercept	E	Pe	$\frac{T_c}{St_e}$
a_i	0.6938 *	0.0087 *	-0.1677 *	0.1521

Third attempt of the regression analysis:

$\Pi = \{E, Pe\}$ and the hypothesized linear relationship is given by the following relation.

$$\hat{U} = a_0 + a_1E + a_2Pe + \epsilon \quad (8)$$

The least-square solution is summarized in Table 5. The condition number is greatly improved. The probability that all $a_i = 0$ at the same time is negligible as seen from the probability of F-statistic. All the coefficients are statistically significant, i.e., the hypothesis that individual $a_i = 0$ can be safely discarded.

Table 5. Third attempt of the regression analysis to estimate the coefficients, a_i , using the linear least-squares approach. Asterisk (*) indicates the statistical significance of the coefficient using a t-test with a 95% confidence interval. Other statistics: $R^2 = 0.746$, Adjusted $R^2 = 0.737$, F-statistic = 83.61, $P(F) = 0.0$. Condition number = 422.

Parameter	Intercept	E	Pe
a_i	0.8146 *	0.0082 *	-0.1654 *

Now, the linear model given by Equation (8) is interpreted in light of the physics of the additive process. The heat received by the material is defined by a quantity \hat{U} . The higher the heat received, the greater the temperature reached by the system. This \hat{U} is related to the various material properties and process parameters. Using the non-dimensional analysis, several parameters were combined into a bunch of non-dimensional numbers. These numbers are associated with and are responsible for several physical phenomena. Using the linear model and the available data, the variation in \hat{U} was explained using a linear combination of constant, E and Pe . A more complete dependence can potentially be highly non-linear, but this also can be analytically intractable.

5. Results

In the previous section, a linear least-squares regression approach was used to arrive at a relation for the dimensionless heat energy absorbed, \hat{U} . The regression analysis resulted in a relation for \hat{U} in terms of the dimensionless power, E , and the Péclet number, (Pe). In the following sections (Sections 5.1–5.3), relation for \hat{U} is used to investigate the advective transport occurring inside the meltpool for different alloys and then to characterize their meltpool morphology (aspect ratio and volume) using the Marangoni number and the Stefan number. In Section 5.4, \hat{U} is used to characterize microstructure evolution using the temperature gradients and the cooling rates in the solidified region.

5.1. Influence of Péclet Number on Advection Transport in the Meltpool

In this section, the extent of advection transport observed in the meltpool in different alloys during the LBPF process is discussed. The goal is to analyze the macroscopic geometric features of the meltpool, such as its aspect ratio and volume. In trying to explain the variation of these macroscopic features, a measure of advection in the meltpool using

the relevant dimensionless quantities are critically investigated. Figure 5 describes the variation of the Péclet number, $Pe^* = Pev_{max}$, with the non-dimensional quantity $Ma\hat{U}$. It is to be noted that the Péclet number with an asterisk, $Pe^* = Pev_{max} = \frac{l_p v_p}{\alpha} \frac{v_{max}}{v_p}$, is defined using the maximum velocity in the melt pool, and is a measure of the advective transport relative to the diffusion transport in the melt pool. A larger value of Pe^* denotes a larger circulation of heat inside the melt pool due to the fluid motion. The dimensionless quantity $Ma^* = Ma\hat{U}$ is a measure of heat transport caused by the fluid flow induced due to the surface tension gradient. As seen from Figure 5, for the alloy shown, Pe^* increase with the Ma^* . This correlation implies the overall movement of fluid in the melt pool is greater if the advection transport due to surface tension force is greater. Each point in these plots represents a single simulation result for the relevant quantities plotted and is obtained from the FEM framework. Another key information conveyed in Figure 5 is that for some alloys such as AlSi10Mg, advection due to surface tension forces is minimal, as can be seen from the numerical values of the total advection (Pev_{max}) shown on the Y-axis. On the other hand, alloys such as Ti6Al4V show a higher value of advection transport due to surface tension forces. These observations are important correlations between advection measure $Pe^* = Pev_{max}$, Marangoni number, Péclet number, and the dimensionless power ($Ma\hat{U} = a_0Ma + a_1MaE + a_2MaPe$), and will be used below to make connections to the melt pool morphology.

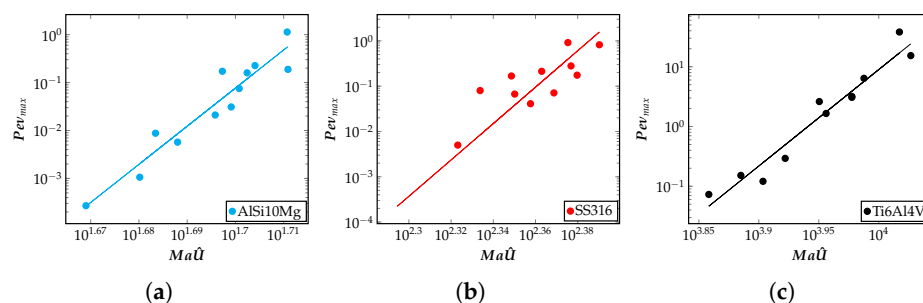


Figure 5. Measure of total advection measured as Pev_{max} vs. surface tension based advection $Ma\hat{U} = a_0Ma + a_1MaE + a_2MaPe$ on a log–log scale for (a) AlSi10Mg, (b) SS316, (c) Ti6Al4V alloys. Corresponding plots comparing IN718 and AZ91D alloys, and a comparison of all the five alloys considered in this work can be found in Figures S1 and S2 of the Supplementary Information, respectively. The advection measure corresponds to the degree of fluid flow inside the melt pool. Each point in these plots represent a single simulation result for the relevant quantities plotted, and is obtained from the FEM framework.

5.2. Influence of Marangoni Number on the Melt pool Aspect Ratio

In this section, the geometric characteristics of the melt pool, particularly the aspect ratio is discussed. The melt pool aspect ratio is defined as the ratio of its maximum length to its maximum width ($\frac{l_m}{w_m}$). To understand aspect ratio in terms of the input process parameters, dimensionless quantity $Ma\hat{U}$ is useful. For characterizing the melt pool shapes, correlations were found between $Ma\hat{U} = a_0Ma + a_1MaE + a_2MaPe$ and the aspect ratio of the melt pool for different alloys, and different process parameters. The rise in \hat{U} is an indication of enough heat received by the material to cause melting during the additive process. The aspect ratio of the melt pool is related to the fluid flow induced inside the melt pool. As shown in the previous section, in Figure 5, AlSi10Mg alloy has a low advection measure, Pev_{max} , and Ti6Al4V alloy has a high advection measure. This information is relevant here to understand the melt pool shapes of these materials. Figure 6a shows the variation of the aspect ratio ($\frac{l_m}{w_m}$) plotted as a function of non-dimensional quantity $Ma\hat{U}$ for Ti6Al4V alloy material. The aspect ratio increases with $Ma\hat{U}$. The aspect ratio with $Ma\hat{U}$ if visualized in a combined plot for all the three alloys considered in this work, it is instructional to see the separations of materials into three clusters—each for one alloy, as seen in Figure 6b. From this clustering, it can be seen that Ti6Al4V almost always

produced an elongated or elliptical-shaped meltpool whose aspect ratio is far from one. The alloy AlSi10Mg produces a meltpool that is relatively less elongated and has an aspect ratio closer to one. The advection in the fluid flow causes the meltpool to expand along the direction of the higher temperature gradient. From this discussion, insightful observations, relating the aspect ratio of the meltpool with $Ma\hat{U}$, can be made that help us characterize the meltpool shapes potentially produced by different alloys.

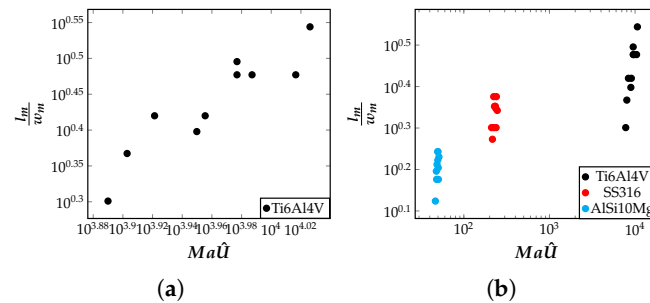


Figure 6. Correlation of the aspect ratio with $Ma\hat{U} = a_0Ma + a_1MaE + a_2MaPe$, plotted on a log–log scale, for (a) Ti6Al4V alloy, and for (b) three alloys (Ti6Al4V, SS316 and AlSi10Mg) shown in a single plot to demonstrate clustering. A combined plot demonstrating this clustering for all the five alloys (Ti6Al4V, SS316, AlSi10Mg, IN718 and AZ91D) considered in this work can be found in Figure S3 of the Supplementary Information. Each point in these plots represent a single simulation result for the relevant quantities plotted, and is obtained from the FEM framework.

5.3. Influence of Stefan Number on Meltpool Volume

In this section, a relation between the input non-dimensional numbers and the volume of the meltpool is presented. The volume of the meltpool is the volume of the localized region where the heat received by the material resulted in the melting of the material. The pool volume is identified using the liquid fraction, ϕ , which is a variable that we track in the model at all time instances and all spatial points in the domain. To completely melt the material, the material needs to absorb enough power to raise the temperature above the liquidus temperature and to overcome the latent heat barrier. The dimensionless power absorbed by the material is associated as a form of latent power, $P_L = \frac{\Omega_m}{l_p^3} \frac{T_c}{Ste}$. Since $\frac{T_c}{Ste}$ is constant for a given material, P_L is proportional to the volume of the material melted ($\tilde{\Omega}_m$). One can expect, as a first-order argument, that more material will melt if \hat{U} is higher. Thus, one can expect $P_L = \tilde{\Omega}_m \frac{T_c}{Ste}$ to increase with \hat{U} . This understanding helps us anticipate that the meltpool volume for different alloys, $\tilde{\Omega}_m$, increases with $\frac{Ste\hat{U}}{T_c}$, and this can indeed be seen in Figure 7a–c. The numerical range of the meltpool volumes across the data points is similar, but for a given alloy, the meltpool volume increases with $\frac{Ste}{T_c} \hat{U}$. With this analysis, an important correlation is obtained between the meltpool volume and the quantity $\frac{Ste}{T_c} \hat{U} = a_0 \frac{Ste}{T_c} + a_1 \frac{SteE}{T_c} + a_2 \frac{StePe}{T_c}$.

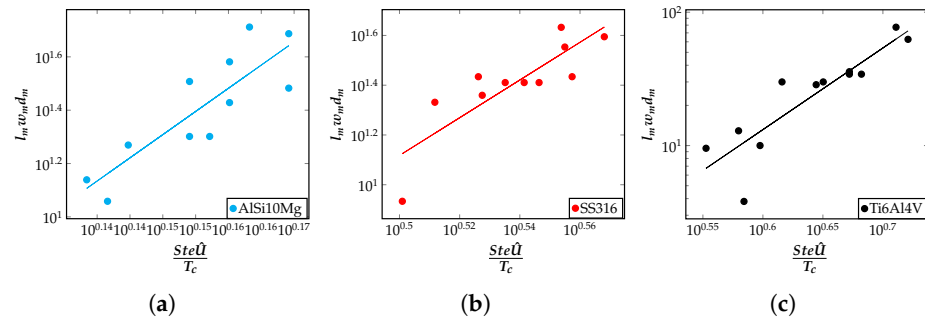


Figure 7. Correlation of the melt pool volume ($I_m w_m d_m$) with $\frac{Ste \hat{U}}{T_c} = a_0 \frac{Ste}{T_c} + a_1 \frac{Ste E}{T_c} + a_2 \frac{Ste Pe}{T_c}$, plotted on a log–log scale, for (a) AlSi10Mg, (b) SS316, and (c) Ti6Al4V alloys. Corresponding plots comparing IN718 and AZ91D alloys, and a comparison of all the five alloys considered in this work can be found in Figure S4 and S5 of the Supplementary Information, respectively. Each point in these plots represent a single simulation result for the relevant quantities plotted, and is obtained from the FEM framework.

5.4. Influence of the Heat Absorbed on the Solidification Cooling Rates

In this section, a discussion on characterizing the microstructure of the solidified region is presented. To support this discussion, \hat{U} is used to explain the variation in the output variables such as the temperature gradient, G , and the cooling rate, Gv_p , where v_p is the laser scan speed. These variables are traditionally understood to have a direct influence on the microstructure in the solidification literature. $\hat{U} = a_0 + a_1 E + a_2 Pe$, has a strong linear correlation with the temperature gradient, G , as shown in Figure 8a–c. Considering the correlations observed in these figures, it can be inferred that the non-dimensional temperature gradient is proportional to the value of \hat{U} . Further, this relation is expressed entirely in terms of input material properties and process parameters.

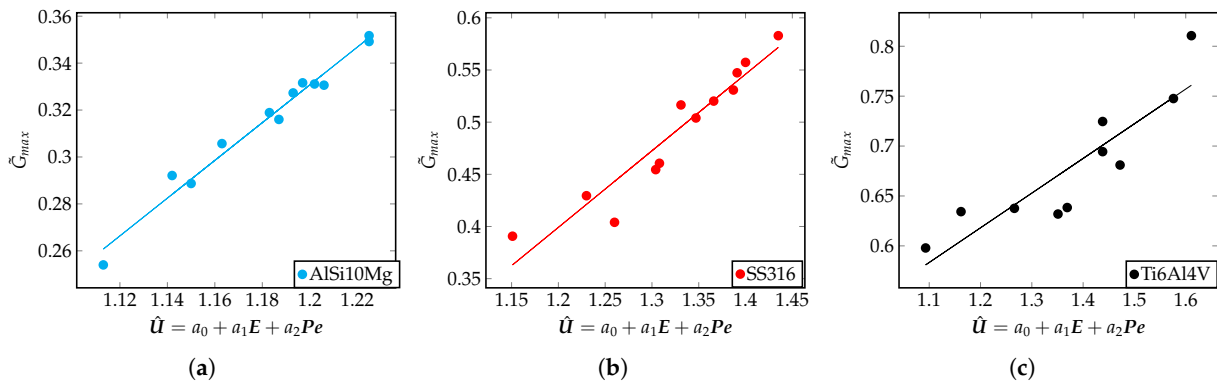


Figure 8. Dimensionless temperature gradient (G) with the \hat{U} for different alloys. Plots corresponding to IN718 and AZ91D alloy material can be found in Figure S6 of the Supplementary Information. Each point in these plots represent a single simulation result for the relevant quantities plotted, and is obtained from the FEM framework.

In the LPBF process, the laser scan speed controls the speed of movement of the solidification interface. The laser scan speed used in the simulations is assumed to be equal to the maximum solid–liquid interface velocity ($v = v_p$ [61,62].) The variation of the cooling rates, Gv_p are observed with \hat{U} by increasing dimensionless laser power, E , but keeping the Péclet number fixed. The dimensionless temperature gradient, \tilde{G}_{max} , will increase with \hat{U} , as seen in Figure 8. It is also instructional to see that the cooling rate, Gv_p , increases with \hat{U} , as shown in Figure 9a. There exists a well-known correlation between a microstructure size, λ_2 , and the cooling rate, Gv_p , in the solidification process, and is given by the relation $\lambda_2 = 25(Gv_p)^{-0.28}$ [60]. Using this relation, it can be seen that the size of

the microstructure will get finer as we increase \hat{U} , which can be achieved by increasing E . Thus, the size of the microstructure correlates with the input non-dimensional quantity given by $\hat{U} = a_0 + a_1E + a_2Pe$.

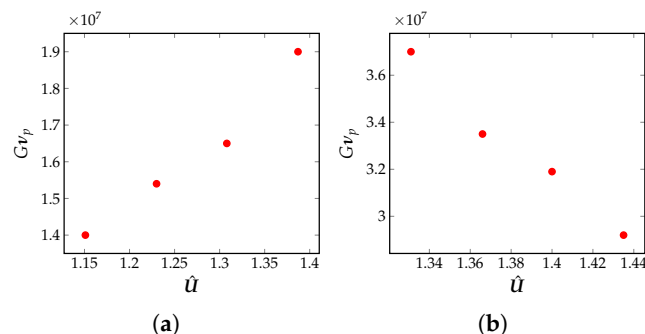


Figure 9. (a) Variation of the dimensional cooling rate, Gv_p , with $\hat{U} = a_0 + a_1E + a_2Pe$, plotted on a log–log scale. Here, \hat{U} is changed by changing E , but keeping Pe fixed for SS316 alloy, (b) Variation of dimensional cooling rate, Gv_p , with $\hat{U} = a_0 + a_1E + a_2Pe$, plotted on a log–log scale. Here, \hat{U} is changed by changing Pe , but keeping E fixed for SS316 alloy.

The effect of \hat{U} on the cooling rate is studied due to a change in the Péclet number, Pe , but keeping the dimensionless laser power, E , fixed. \hat{U} decreases with increase in Pe and E fixed. From Figure 8, it is known that the dimensionless temperature gradient, G , and its dimensional counterpart, both decrease if we decrease \hat{U} . Thus, the cooling rate, Gv_p , decreases with increase in \hat{U} , as seen in Figure 9b. This decrease is solely due to an increase in the value of Pe . Using this information, a correlation is identified between the change in the size of the microstructure and the Péclet number, i.e., increasingly coarser microstructural features can be observed with a decrease in the cooling rate.

6. Conclusions

In this work, the melt pool dynamics of the laser powder bed fusion (LPBF) process are numerically modeled and connections are drawn to important dimensionless quantities influencing the thermo-fluidic evolution of the melt pool and its morphology. Processes such as the interaction of the moving laser power source with the powdered metal, formation of the melt pool, its subsequent solidification, etc., make LPBF a highly coupled multiphysics process. To investigate the multiphysics interactions, the thermo-fluidic governing equations relevant to the LPBF process are numerically modeled using a Finite Element Method (FEM) framework. The simulation predictions were validated by comparing with available results from the literature and with experimental observations of the cooling rates available from our experimental collaborators. Using the classical Buckingham- π theorem and a careful choice of relevant characteristic quantities, the governing equations were reduced to their dimensionless form. Using the dimensionless form and the FEM simulations, an important dimensionless quantity, interpreted as the heat absorbed by the metal powder and the melt pool, is identified. Around 60 different cases of the LPBF process were simulated by varying the alloy type and process conditions, and the simulation data were used to obtain an explicit form of the dimensionless heat absorbed in terms of the input dimensionless numbers using the method of linear least-squares regression. Using physics-based and statistical arguments, a linear model showing dependence of the heat absorbed on the Péclet number and the dimensionless power is established.

The measure of advection inside the melt pool is quantified in terms of the Péclet and the Marangoni numbers and it is found that materials such as Ti-6Al-4V show greater advection, represented by Pe^* , and an elongated elliptical melt pool. Materials such as AlSi10Mg show the least advection and whereas SS316 shows moderate amount of advection. It was found that the melt pool volume of materials such as Ti-6Al-4V, SS316, and AlSi10Mg increases with the product of Stefan number and dimensionless measure of heat absorbed. Solidification cooling rates decrease with the measure of heat absorbed if the

Péclet number is reduced while keeping dimensionless power fixed. This characterization of the meltpool morphology using classical dimensionless numbers and the impact of dimensionless power and Péclet number on the solidification cooling rates presents a novel contribution of this work.

In a future work, potential extension of this dimensional analysis framework to investigate meltpool characteristics such as keyhole formation and microstructural features such as grain morphology in the solidified meltpool region will be explored.

Supplementary Materials: The following supporting information can be downloaded at: <https://www.mdpi.com/article/10.3390/ma16010094/s1>, Table S1: Average material properties for alloys. Table S2: Process conditions for alloys. Figure S1: Measure of total advection measured (Pe_{vmax}) vs surface tension based advection $Ma\hat{U}$ for IN718 and AZ91D. Figure S2: Measure of total advection measured (Pe_{vmax}) vs surface tension based advection $Ma\hat{U}$ for all materials in a combined plot. Figure S3: Correlation of the aspect ratio with $Ma\hat{U}$ for all alloys in a combined plot. Figure S4: Correlation of the meltpool volume with $\frac{Ste\hat{U}}{T_c}$ for IN718 and AZ91D. Figure S5: Correlation of the meltpool volume with $\frac{Ste\hat{U}}{T_c}$ for all alloys in a combined plot. Figure S6: Dimensionless temperature gradient (G) with the \hat{U} for IN718 and AZ91D alloy.

Author Contributions: Conceptualization, K.B. and S.R.; methodology, K.B. and S.R.; software, K.B.; validation, K.B.; formal analysis, K.B.; investigation, K.B.; resources, S.R.; writing—original draft preparation, K.B. and S.R.; writing—review and editing, K.B. and S.R.; visualization, K.B.; supervision, S.R.; project administration, S.R. All authors have read and agreed to the published version of the manuscript.

Funding: This research received no external funding.

Institutional Review Board Statement: Not applicable.

Informed Consent Statement: Not applicable.

Data Availability Statement: Not applicable.

Acknowledgments: The authors would like to thank Dan Thoma (University of Wisconsin-Madison) and Kaila Bertsch (University of Wisconsin-Madison; now at Lawrence Livermore National Laboratory) for very useful discussions on microstructure evolution during the LPBF process, and for providing the experimental data on cooling rates that are shown in Figure 3.

Conflicts of Interest: The authors declare no conflict of interest.

References

1. Huang, Y.; Leu, M.C.; Mazumder, J.; Donmez, A. Additive manufacturing: Current state, future potential, gaps and needs, and recommendations. *J. Manuf. Sci. Eng.* **2015**, *137*, 014001. [[CrossRef](#)]
2. Gibson, I.; Rosen, D.W.; Stucker, B.; Khorasani, M. *Additive Manufacturing Technologies*; Springer: Berlin/Heidelberg, Germany, 2021; Volume 17.
3. Konda Gokuldoss, P.; Kolla, S.; Eckert, J. Additive manufacturing processes: Selective laser melting, electron beam melting and binder jetting—Selection guidelines. *Materials* **2017**, *10*, 672. [[CrossRef](#)] [[PubMed](#)]
4. Wang, Y.M.; Voisin, T.; McKeown, J.T.; Ye, J.; Calta, N.P.; Li, Z.; Zeng, Z.; Zhang, Y.; Chen, W.; Roehling, T.T.; et al. Additively manufactured hierarchical stainless steels with high strength and ductility. *Nat. Mater.* **2018**, *17*, 63–71. [[CrossRef](#)] [[PubMed](#)]
5. Qian, M.; Xu, W.; Brandt, M.; Tang, H. Additive manufacturing and postprocessing of Ti-6Al-4V for superior mechanical properties. *MRS Bull.* **2016**, *41*, 775–784. [[CrossRef](#)]
6. Rittinghaus, S.K.; Jäggle, E.A.; Schmid, M.; Gökce, B. New Frontiers in Materials Design for Laser Additive Manufacturing. *Materials* **2022**, *15*, 6172. [[CrossRef](#)]
7. King, W.E.; Anderson, A.T.; Ferencz, R.M.; Hodge, N.E.; Kamath, C.; Khairallah, S.A.; Rubenchik, A.M. Laser powder bed fusion additive manufacturing of metals; Physics, computational, and materials challenges. *Appl. Phys. Rev.* **2015**, *2*, 041304. [[CrossRef](#)]
8. Fox, J.C.; Moylan, S.P.; Lane, B.M. Effect of process parameters on the surface roughness of overhanging structures in laser powder bed fusion additive manufacturing. *Procedia Cirp* **2016**, *45*, 131–134. [[CrossRef](#)]
9. Dinovitzer, M.; Chen, X.; Laliberte, J.; Huang, X.; Frei, H. Effect of wire and arc additive manufacturing (WAAM) process parameters on bead geometry and microstructure. *Addit. Manuf.* **2019**, *26*, 138–146. [[CrossRef](#)]
10. Ning, F.; Cong, W.; Hu, Y.; Wang, H. Additive manufacturing of carbon fiber-reinforced plastic composites using fused deposition modeling: Effects of process parameters on tensile properties. *J. Compos. Mater.* **2017**, *51*, 451–462. [[CrossRef](#)]

11. Makoana, N.W.; Yadroitsava, I.; Möller, H.; Yadroitsev, I. Characterization of 17-4PH single tracks produced at different parametric conditions towards increased productivity of LPBF systems—The effect of laser power and spot size upscaling. *Metals* **2018**, *8*, 475. [[CrossRef](#)]
12. Letenneur, M.; Kreitzberg, A.; Brailovski, V. Optimization of laser powder bed fusion processing using a combination of melt pool modeling and design of experiment approaches: Density control. *J. Manuf. Mater. Process.* **2019**, *3*, 21. [[CrossRef](#)]
13. Mirkoohi, E.; Ning, J.; Bocchini, P.; Fergani, O.; Chiang, K.N.; Liang, S.Y. Thermal modeling of temperature distribution in metal additive manufacturing considering effects of build layers, latent heat, and temperature-sensitivity of material properties. *J. Manuf. Mater. Process.* **2018**, *2*, 63. [[CrossRef](#)]
14. Mirkoohi, E.; Seivers, D.E.; Garmestani, H.; Liang, S.Y. Heat source modeling in selective laser melting. *Materials* **2019**, *12*, 2052. [[CrossRef](#)] [[PubMed](#)]
15. Mondal, S.; Gwynn, D.; Ray, A.; Basak, A. Investigation of melt pool geometry control in additive manufacturing using hybrid modeling. *Metals* **2020**, *10*, 683. [[CrossRef](#)]
16. Abolhasani, D.; Seyedkashi, S.H.; Kang, N.; Kim, Y.J.; Woo, Y.Y.; Moon, Y.H. Analysis of melt-pool behaviors during selective laser melting of AISI 304 stainless-steel composites. *Metals* **2019**, *9*, 876. [[CrossRef](#)]
17. Ansari, M.J.; Nguyen, D.S.; Park, H.S. Investigation of SLM process in terms of temperature distribution and melting pool size: Modeling and experimental approaches. *Materials* **2019**, *12*, 1272. [[CrossRef](#)]
18. Dong, Z.; Liu, Y.; Wen, W.; Ge, J.; Liang, J. Effect of hatch spacing on melt pool and as-built quality during selective laser melting of stainless steel: Modeling and experimental approaches. *Materials* **2018**, *12*, 50. [[CrossRef](#)]
19. Ansari, P.; Rehman, A.U.; Pitir, F.; Veziroglu, S.; Mishra, Y.K.; Aktas, O.C.; Salamci, M.U. Selective laser melting of 316L austenitic stainless steel: Detailed process understanding using multiphysics simulation and experimentation. *Metals* **2021**, *11*, 1076. [[CrossRef](#)]
20. Gusarov, A.; Yadroitsev, I.; Bertrand, P.; Smurov, I. Heat transfer modelling and stability analysis of selective laser melting. *Appl. Surf. Sci.* **2007**, *254*, 975–979. [[CrossRef](#)]
21. Mukherjee, T.; Wei, H.; De, A.; DebRoy, T. Heat and fluid flow in additive manufacturing—Part I: Modeling of powder bed fusion. *Comput. Mater. Sci.* **2018**, *150*, 304–313. [[CrossRef](#)]
22. Khairallah, S.A.; Anderson, A. Mesoscopic simulation model of selective laser melting of stainless steel powder. *J. Mater. Process. Technol.* **2014**, *214*, 2627–2636. [[CrossRef](#)]
23. Wang, Z.; Yan, W.; Liu, W.K.; Liu, M. Powder-scale multi-physics modeling of multi-layer multi-track selective laser melting with sharp interface capturing method. *Comput. Mech.* **2019**, *63*, 649–661. [[CrossRef](#)]
24. Keshavarzkermani, A.; Marzbanrad, E.; Esmaeilzadeh, R.; Mahmoodkhani, Y.; Ali, U.; Enrique, P.D.; Zhou, N.Y.; Bonakdar, A.; Toyserkani, E. An investigation into the effect of process parameters on melt pool geometry, cell spacing, and grain refinement during laser powder bed fusion. *Opt. Laser Technol.* **2019**, *116*, 83–91. [[CrossRef](#)]
25. Fayazfar, H.; Salarian, M.; Rogalsky, A.; Sarker, D.; Russo, P.; Paserin, V.; Toyserkani, E. A critical review of powder-based additive manufacturing of ferrous alloys: Process parameters, microstructure and mechanical properties. *Mater. Des.* **2018**, *144*, 98–128. [[CrossRef](#)]
26. Ruzicka, M. On dimensionless numbers. *Chem. Eng. Res. Des.* **2008**, *86*, 835–868. [[CrossRef](#)]
27. Van Elsen, M.; Al-Bender, F.; Kruth, J.P. Application of dimensional analysis to selective laser melting. *Rapid Prototyp. J.* **2008**, *14*, 15–22. [[CrossRef](#)]
28. Islam, Z.; Agrawal, A.K.; Rankouhi, B.; Magnin, C.; Anderson, M.H.; Pfefferkorn, F.E.; Thoma, D.J. A high-throughput method to define additive manufacturing process parameters: Application to Haynes 282. *Metall. Mater. Trans. A* **2022**, *53*, 250–263. [[CrossRef](#)]
29. Weaver, J.S.; Heigel, J.C.; Lane, B.M. Laser spot size and scaling laws for laser beam additive manufacturing. *J. Manuf. Process.* **2022**, *73*, 26–39. [[CrossRef](#)]
30. Rankouhi, B.; Agrawal, A.K.; Pfefferkorn, F.E.; Thoma, D.J. A dimensionless number for predicting universal processing parameter boundaries in metal powder bed additive manufacturing. *Manuf. Lett.* **2021**, *27*, 13–17. [[CrossRef](#)]
31. Gan, Z.; Kafka, O.L.; Parab, N.; Zhao, C.; Fang, L.; Heinonen, O.; Sun, T.; Liu, W.K. Universal scaling laws of keyhole stability and porosity in 3D printing of metals. *Nat. Commun.* **2021**, *12*, 2379. [[CrossRef](#)]
32. Wang, Z.; Liu, M. Dimensionless analysis on selective laser melting to predict porosity and track morphology. *J. Mater. Process. Technol.* **2019**, *273*, 116238. [[CrossRef](#)]
33. Noh, J.; Lee, J.; Seo, Y.; Hong, S.; Kwon, Y.S.; Kim, D. Dimensionless parameters to define process windows of selective laser melting process to fabricate three-dimensional metal structures. *Opt. Laser Technol.* **2022**, *149*, 107880. [[CrossRef](#)]
34. Ahsan, F.; Razmi, J.; Ladani, L. Global local modeling of melt pool dynamics and bead formation in laser bed powder fusion additive manufacturing using a multi-physics thermo-fluid simulation. *Prog. Addit. Manuf.* **2022**, *7*, 1275–1285. [[CrossRef](#)]
35. Wu, J.; Zheng, X.; Zhang, Y.; Ren, S.; Yin, C.; Cao, Y.; Zhang, D. Modeling of whole-phase heat transport in laser-based directed energy deposition with multichannel coaxial powder feeding. *Addit. Manuf.* **2022**, *59*, 103161. [[CrossRef](#)]
36. Cardaropoli, F.; Alfieri, V.; Caiazzo, F.; Sergi, V. Dimensional analysis for the definition of the influence of process parameters in selective laser melting of Ti–6Al–4V alloy. *Proc. Inst. Mech. Eng. Part B J. Eng. Manuf.* **2012**, *226*, 1136–1142. [[CrossRef](#)]
37. Mukherjee, T.; Manvatkar, V.; De, A.; DebRoy, T. Dimensionless numbers in additive manufacturing. *J. Appl. Phys.* **2017**, *121*, 064904. [[CrossRef](#)]

38. Robert, A.; Debroy, T. Geometry of laser spot welds from dimensionless numbers. *Metall. Mater. Trans. B* **2001**, *32*, 941–947. [[CrossRef](#)]
39. Lu, S.; Fujii, H.; Nogi, K. Sensitivity of Marangoni convection and weld shape variations to welding parameters in O₂-Ar shielded GTA welding. *Scr. Mater.* **2004**, *51*, 271–277. [[CrossRef](#)]
40. Wei, P.; Ting, C.; Yeh, J.; DebRoy, T.; Chung, F.; Yan, G. Origin of wavy weld boundary. *J. Appl. Phys.* **2009**, *105*, 053508. [[CrossRef](#)]
41. Asztalos, Z.; Száva, I.; Vlase, S.; Száva, R.I. Modern Dimensional Analysis Involved in Polymers Additive Manufacturing Optimization. *Polymers* **2022**, *14*, 3995. [[CrossRef](#)]
42. Chia, H.Y.; Wu, J.; Wang, X.; Yan, W. Process parameter optimization of metal additive manufacturing: A review and outlook. *J. Mater. Inform.* **2022**, *2*, 16. [[CrossRef](#)]
43. Bhagat, K.; Rudraraju, S. Modeling of dendritic solidification and numerical analysis of the phase-field approach to model complex morphologies in alloys. *Eng. Comput.* **2022**, 1–19. [[CrossRef](#)]
44. Brent, A.; Voller, V.R.; Reid, K. Enthalpy-porosity technique for modeling convection-diffusion phase change: Application to the melting of a pure metal. *Numer. Heat Transf. Part A Appl.* **1988**, *13*, 297–318.
45. Kumar, A.; Roy, S. Effect of three-dimensional melt pool convection on process characteristics during laser cladding. *Comput. Mater. Sci.* **2009**, *46*, 495–506. [[CrossRef](#)]
46. Yarin, L.P. *The Pi-Theorem: Applications to Fluid Mechanics and Heat and Mass Transfer*; Springer Science & Business Media: Berlin/Heidelberg, Germany, 2012; Volume 1.
47. Curtis, W.; Logan, J.D.; Parker, W. Dimensional analysis and the pi theorem. *Linear Algebra Its Appl.* **1982**, *47*, 117–126. [[CrossRef](#)]
48. Bluman, G.W.; Kumei, S. *Symmetries and Differential Equations*; Springer Science & Business Media: Berlin/Heidelberg, Germany, 2013; Volume 81.
49. Hughes, T.J. *The Finite Element Method: Linear Static and Dynamic Finite Element Analysis*; Courier Corporation: Gloucester, MA, USA, 2012.
50. Arndt, D.; Bangerth, W.; Blais, B.; Fehling, M.; Gassmöller, R.; Heister, T.; Heltai, L.; Köcher, U.; Kronbichler, M.; Maier, M.; et al. The deal.II Library, Version 9.3. *J. Numer. Math.* **2021**, *29*, 171–186. [[CrossRef](#)]
51. Chorin, A.J. A numerical method for solving incompressible viscous flow problems. *J. Comput. Phys.* **1997**, *135*, 118–125. [[CrossRef](#)]
52. Gulati, R.; Rudraraju, S. Spatio-temporal modeling of saltatory conduction in neurons using Poisson-Nernst-Planck treatment and estimation of conduction velocity. *Brain Multiphys.* **2022**, *4*, 100061. [[CrossRef](#)]
53. Wang, Z.; Rudraraju, S.; Garikipati, K. A three dimensional field formulation, and isogeometric solutions to point and line defects using Toupin’s theory of gradient elasticity at finite strains. *J. Mech. Phys. Solids* **2016**, *94*, 336–361. [[CrossRef](#)]
54. Jiang, T.; Rudraraju, S.; Roy, A.; Van der Ven, A.; Garikipati, K.; Falk, M.L. Multiphysics simulations of lithiation-induced stress in $Li_{1+x}Ti_2O_4$ electrode particles. *J. Phys. Chem. C* **2016**, *120*, 27871–27881. [[CrossRef](#)]
55. Rudraraju, S.; Moulton, D.E.; Chirat, R.; Goriely, A.; Garikipati, K. A computational framework for the morpho-elastic development of molluscan shells by surface and volume growth. *PLoS Comput. Biol.* **2019**, *15*, e1007213. [[CrossRef](#)] [[PubMed](#)]
56. Bhagat, K. Meltpool Thermo-Fluidics Simulation Framework for Metal Additive Manufacturing. 2022. Available online: <https://github.com/cmmg/AMMeltpoolThermoFluidics> (accessed on 19 December 2022).
57. Bertsch, K.; De Bellefon, G.M.; Kuehl, B.; Thoma, D. Origin of dislocation structures in an additively manufactured austenitic stainless steel 316L. *Acta Mater.* **2020**, *199*, 19–33. [[CrossRef](#)]
58. Shen, H.; Yan, J.; Niu, X. Thermo-fluid-dynamic modeling of the melt pool during selective laser melting for AZ91D magnesium alloy. *Materials* **2020**, *13*, 4157. [[CrossRef](#)] [[PubMed](#)]
59. Rankouhi, B.; Bertsch, K.; de Bellefon, G.M.; Thevamaran, M.; Thoma, D.; Suresh, K. Experimental validation and microstructure characterization of topology optimized, additively manufactured SS316L components. *Mater. Sci. Eng. A* **2020**, *776*, 139050. [[CrossRef](#)]
60. Thoma, D.; Charbon, C.; Lewis, G.; Nemeč, R. Directed light fabrication of iron-based materials. *MRS Online Proc. Libr. Arch.* **1995**, *397*, 341–346. [[CrossRef](#)]
61. Mohammadpour, P.; Plotkowski, A.; Phillion, A.B. Revisiting solidification microstructure selection maps in the frame of additive manufacturing. *Addit. Manuf.* **2020**, *31*, 100936. [[CrossRef](#)]
62. Rappaz, M.; David, S.; Vitek, J.; Boatner, L. Analysis of solidification microstructures in Fe-Ni-Cr single-crystal welds. *Metall. Trans. A* **1990**, *21*, 1767–1782. [[CrossRef](#)]

Disclaimer/Publisher’s Note: The statements, opinions and data contained in all publications are solely those of the individual author(s) and contributor(s) and not of MDPI and/or the editor(s). MDPI and/or the editor(s) disclaim responsibility for any injury to people or property resulting from any ideas, methods, instructions or products referred to in the content.